PVDF-HFP/PVP-based Miscible Blend Electrolyte for Fast-Charging Lithium Metal Batteries

*Pratiksha Gami, Asish Kumar Das, Hari Narayanan Vasavan, Samriddhi Saxena, Neha Dagar, and Sunil Kumar**

Department of Metallurgical Engineering and Materials Science, Indian Institute of Technology Indore, Simrol, 453552, India.

*Corresponding author, E-mail: sunil@iiti.ac.in

Keywords: Fast-charging Li metal battery, miscible blend electrolyte, ionic conductivity, electrochemical stability

Abstract

Polymer electrolytes, with their excellent mechanical properties, processability, and electrochemical stability, are gaining attention for their potential in lithium metal batteries. This study introduces a solid-state polymer electrolyte synthesized through a supramolecular approach, utilizing poly(vinylidene fluoride hexafluorophosphate) (PVDF-HFP) and polyvinylpyrrolidone (PVP) in conjunction with lithium bis(trifluoromethanesulfonyl)imide (LiTFSI) salt. The F-containing segments in PVDF-HFP establish hydrogen bonds with the carbonyl groups in PVP, resulting in a cross-linked supramolecular network that facilitates rapid Li-ion conduction in polymer electrolytes. The developed electrolyte delivers an impressive ionic conductivity of 2.84 $\times$ 10^{-4} S cm^{-1} and a high Li-ion transference number of ~0.44. The electrolyte film is electrochemically stable up to ~4.53 V. Notably, symmetric Li||Li cells exhibit stable cycling for over 1500 cycles (1 mA cm^{-2}), and an excellent critical current density of 6 mA cm^{-2} is observed, demonstrating the compatibility of optimized polymer electrolytes with lithium metal anodes. Furthermore, Li||$LiFePO_4$ full-cell delivers a ~70 mAh g^{-1} capacity with >99% retention after 200 cycles at 5C. This novel multi-pathway blend of fast lithium-conducting polymers enhances safety and energy density, and its robust performance has significant potential for widespread implementation in solid-state lithium metal batteries.

1. Introduction

Under rising environmental and regulatory demands, the global transition to electrifying vehicles has become crucial. [1] Electric vehicles (EVs) that run entirely on batteries are now among one of the most desirable categories of "green" automobiles. [2] Among all the obstacles to the widespread adoption of electric vehicles, one of the hardest for customers and researchers to overcome is the longer charging period. [3] While refueling a car with an internal combustion engine typically takes only a few minutes, the fastest charging time for an electric vehicle is around 30 minutes to reach an 80% state of charge (SOC). [3a] Fast charging has been seen as one of the most essential avenues for advancing EVs in the market and, therefore, in battery research. [4]

Lithium metal batteries (LMBs) using liquid electrolytes offer greater energy density than Li-ion batteries. [5] However, the growth of lithium dendrites can lead to internal short circuits, creating significant safety risks. [6] In contrast, solid electrolyte-based lithium batteries offer better energy density and safety. [7] Solid organic electrolytes (SOEs) have garnered substantial interest among various Li-conducting solid-state conductors because of their physicochemical properties (e.g., high flexibility and ease of thin-film fabrication). [8] Nonetheless, the ionic conductivity of SOEs is significantly hindered by the tangling of polymer chains or the interaction with anions, especially at room temperature, rendering their practical deployment unfeasible. [8d] Therefore, developing polymer blends has become vital for Li-conducting electrolyte membranes with customized features. [9]

Macromolecular blends encompassing PEO-based electrolytes are well-known for their low glass transition temperature and high solubility for lithium salts. [10] However, the strong interactions between the ethylene oxide (EO) segments and Li^+ lead to a low transference number for lithium ions. [9a, 11] In comparison, PVP polymers offer better biocompatibility, film-forming properties,

and the capacity to produce transparent, self-standing films while water-soluble. [12] PVP also interacts well with other polymers and reagents due to its weak basicity and capacity to form hydrogen bonds. [13] Copolymers like PVDF-HFP are widely used in polymer electrolytes for their mechanical flexibility and robustness. [14] The PVDF-HFP/PVP blend provides an optimal balance of mechanical strength, thermal stability, enhanced ionic conductivity, and processing versatility, making it a promising candidate for next-generation battery applications. [12b]

In this study, polymer blends comprising PVDF-HFP and PVP were synthesized with LiTFSI as a Li-ion conducting entity. The blend possesses high Li-ion conductivity due to the integrated functional characteristics of the C-F of PVDF-HFP and amide moieties of PVP. The high electronegativity and efficient electron-absorbing capabilities of fluorine in PVDF-HFP allowed for multichannel lithium-ion conduction in this solid-state polymer electrolyte. The optimized composition of the solid-state polymer electrolyte was determined to be (75:25) PVDF-HFP:PVP, which exhibited a high ionic conductivity of 2.84×10^{-4} S cm^{-1} and a lithium-ion transference number (t_{Li^+}) of 0.44 at room temperature (RT). The choice of optimum blend composition (PVDF-HFP:PVP in 75:25 ratio) is based on findings of our detailed work on the structural, thermal, and electrical properties of the PVDF-HFP:PVP blend system, which is under peer review. A consistent lithium plating/stripping across the polymer electrolyte was accomplished for 1500 cycles at a current density of 1 mA cm^{-2}. The absence of lithium dendrite growth during prolonged cycling is linked to establishing a stable interfacial layer. Furthermore, the solid-state organic electrolyte demonstrates a wide electrochemical stability window of 4.53 V. Finally, to investigate the rate capabilities and viability of polymer electrolyte additions in next-generation LMBs, Li||$LiFePO_4$ full-cells were tested at different current densities. This innovative architecture creates new opportunities in the quest for the next-generation, fast-charging solid-state lithium metal batteries.

2. Results and discussion

Figure 1 shows the XRD patterns of PE*x* polymer blends with various weight percentages of LiTFSI. Two broad humps at 2θ ~19° and ~38° can be observed in the PVDF-HFP/PVP blend film's XRD patterns (Fig. 1). Two peaks at ~18° and 21° in the XRD pattern for PE0 are attributed to the (100) and (020) peaks of PE0. [12b] As LiTFSI content increased, the relative intensity of the (100) peak became lesser and lesser, confirming its effective integration and compatibility in the polymer blend matrix. [15] This finding confirms that the amorphous regions are uniformly distributed within the host matrix, indicating the semi-crystalline structure of the (PVDF-HFP/PVP)/LiTFSI composite, which can lead to enhanced ionic conductivity and increased ionic diffusivity. [16] Thus, the XRD analysis confirms the formation of LiTFSI and PVDF-HFP/PVP complexes in these films.

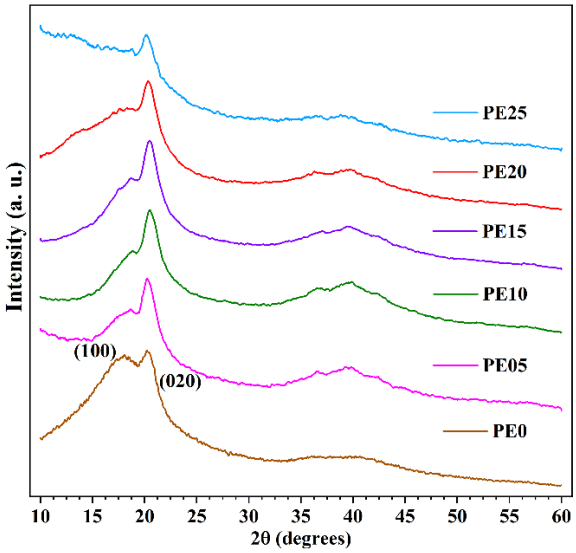

Figure 1 XRD patterns of PE0, PE05, PE10, PE15, PE20 and PE25.

FTIR spectroscopy is an invaluable tool for examining polymer structures, offering insights into the interactions and complexations among the various components of polymer electrolyte membranes. The FTIR spectra of the PVDF-HFP/PVP blend and PE*x* polymer blend electrolyte

films are presented in **Figure 2**. The FTIR spectrum of the PVDF-HFP/PVP (75/25) blend exhibits a broad band at 1655 cm^{-1}, linked to hydrogen bonding or dipole-dipole interactions between two polymer entities. [17] The intensity of this peak increases with lithium salt addition, suggesting enhanced secondary interactions between the polymer blend and the salt. A distinct band at 1056 cm^{-1} in the FTIR spectrum of the PVDF-HFP/PVP blend corresponds to the stretching vibration of the C-O group. The 840 and 1401 cm^{-1} bands correspond to CH_2 bending and wagging vibrations, respectively. The band at 1295 cm^{-1}, corresponding to C-N stretching vibrations of PVP, is also seen in the FTIR spectra of the polymer blend film. [18] A band at 1353 cm^{-1} confirms CH_2 wagging within the blend polymers. [12a] The peaks at 1177 cm^{-1} belong to C-F asymmetric stretching. The FTIR bands at 872 cm^{-1} indicate the presence of the γ-phase in the PVDF-HFP. [19] The mixed mode of molecular vibrations at 840 cm^{-1} indicates the β-phase of PVDF-HFP, -CH_2- rocking, and -CF_2- stretching. [20] A peak at 742 cm^{-1} indicates a mixed mode of vibrations of S-N-S interactions from Li-salt and C-H wagging vibration of the imidazolium ring in PVP. [21] The orange region corresponds to the stretching vibrations of CF_3, while the yellow area is associated with the bending vibrations of SO_2 of the Li-conductor. [21] The peak corresponding to 657 cm^{-1} is related to C-H vibrations. The FTIR spectrum of the PE blend film demonstrates the miscibility of both polymers, attributed to hydrogen bonding interactions between the fluoride groups of PVDF-HFP and the carbonyl group of PVP. The alterations of peaks in the FTIR spectra of polymer blend electrolyte films provide direct proof of complex formation between the polymers and LiTFSI salt. [22]

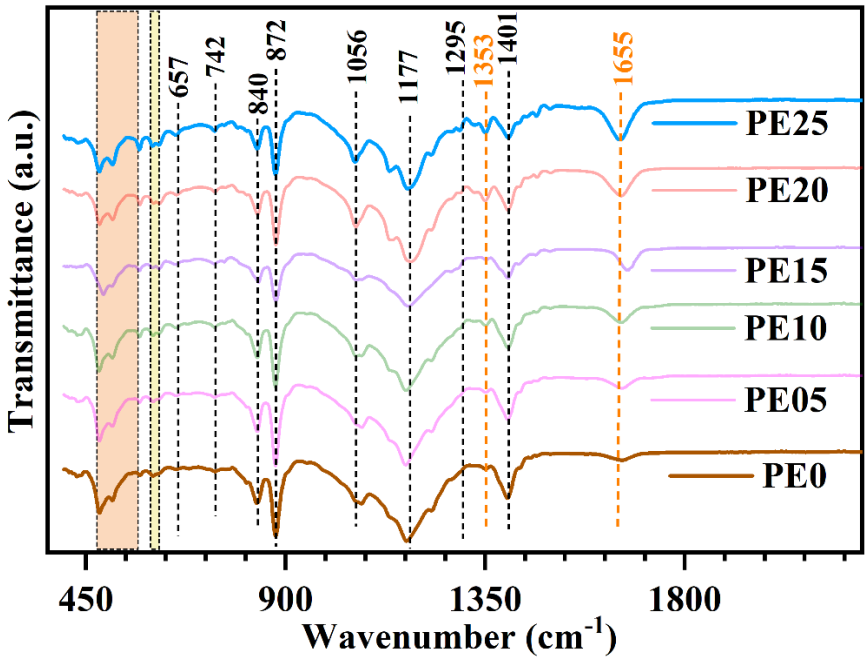

Figure 2 FTIR spectra of PE0, PE05, PE10, PE15, PE20 and PE25.

Field-emission scanning electron microscopy (FE-SEM) was used to investigate the microstructure and surface morphology of PE*x* polymer blend electrolyte films. **Figure 3 and S1-S4** show the SEM micrographs of the polymer blend electrolyte films. Scanning electron micrographs of pure PVDF-HFP/PVP blend films show a smooth, homogeneous surface morphology. Figures 3(a)-(b) and S1-S3 show that smooth surfaces were found up to PE20, indicating the complete miscibility of the salt in the polymer blend. The segregated particles were noticed in the PE25 film, signifying a phase separation or partial miscibility of the different phases, as reflected in Fig. S4. [12b] Figure 3(b1-b5) illustrates that the elements (C, F, N, O, and S) are evenly distributed across the polymer film PE20. XRD investigation indicates that the amorphous region is more prominent in PE*x* electrolytes. Thus, the scanning electron microscopy findings are consistent with the FTIR and XRD analyses.

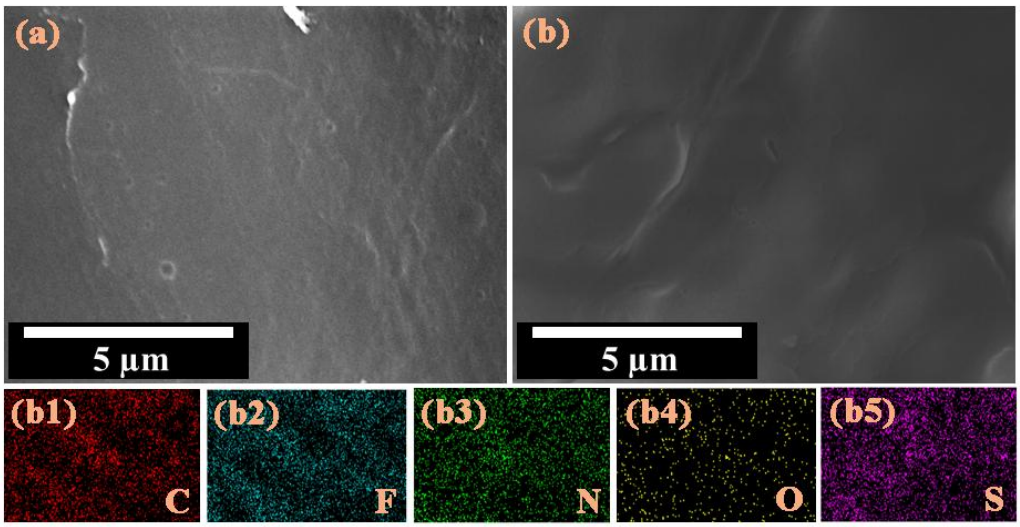

Figure 3 SEM micrographs of (a) PE0, (b) PE20, and EDS elemental mappings of PE20 (b1-b5).

The lithium-ion conductivity of the PE*x* electrolytes was assessed using electrochemical impedance spectroscopy (EIS) with stainless steel (SS) electrodes. The resulting Nyquist plots displayed semicircles at higher frequencies, along with a connected inclined tail in the low-frequency region (**Figure 4(a)-(f)**). Figure 4(a) illustrates an EIS spectrum of PE0 in which only a big semicircular arc is observed, and the spectrum was fitted with an equivalent circuit CPE||R (CPE denotes constant-phase element, and R denotes total resistance). This confirmed the very high resistance of the polymer film. In Fig. 4(b)-(f), the low-frequency tail is due to the Li-ion-blocking SS electrodes in PE05-PE25 samples, and its intercept on the Z'-axis reflects the total resistance of the PEx electrolyte membranes. As the lithium salt concentration increased, the PE*x* electrolytes' resistance decreased to the PE20 film but increased again for PE25. The Nyquist plots were fitted to an equivalent circuit (CPE1||R) + (CPE2) to investigate the reasons behind this trend. The total ionic conductivity and resistance obtained from the fitting process for all the electrolyte membranes are summarized in Table 1 in the supplementary material. The PE20 has the lowest resistance value of 21 Ω (corresponding highest ionic conductivity of 2.84×10^{-4} S cm^{-1}) at room

temperature. Upon further lithium salt addition, the total ionic conductivity of PE25 has decreased. This behavior is attributed to the formation of ion pairs or ion triplets or ion segregation, which restrict the movement of free ions and, consequently, reduce the overall ionic conductivity [15, 16b, 23]. Figure S5 illustrates the logarithmic conductivity *vs.* 1000/T plot, allowing for calculating the activation energy for lithium-ion conduction, which was found to be ~ 0.39 eV using the Arrhenius equation (equation S1). This low activation energy suggests efficient lithium-ion migration within the polymer electrolyte.

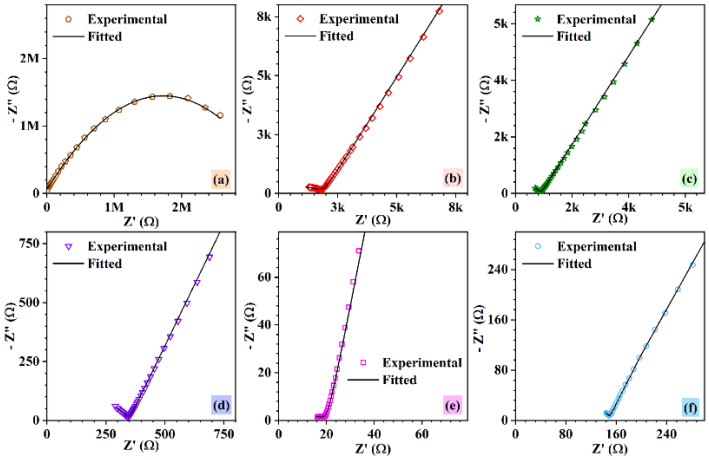

Figure 4 Room temperature Nyquist plots of (a) PE0, (b) PE05, (c) PE10, (d) PE15, (e) PE20, and (f) PE25. Impedance data of PE0 is fitted with an equivalent circuit of (CPE||R), and those of samples (PE05-PE25) are fitted with an equivalent circuit (CPE1||R) + (CPE2).

Table 1. The total resistance and ionic conductivity of PE0-PE25 films at room temperature were calculated using the equivalent circuit fitting.

Sample	Total Resistance	Total conductivity (S cm^{-1})
PE0	3.5 MΩ	8.57×10^{-10}
PE05	1943 Ω	3.07×10^{-6}
PE10	811 Ω	7.36×10^{-6}

PE15	347 Ω	1.72×10^{-5}
PE20	21 Ω	2.84×10^{-4}
PE25	141 Ω	4.23×10^{-5}

One of the most critical factors determining the practicality of polymer blend electrolytes in lithium metal batteries is their thermal stability. Thermogravimetric analysis (TGA) was used to assess the thermal stability of electrolyte films. **Figure 5(a)** shows the TGA plot of the polymer blend electrolyte film doped with 20 wt% LITFSI salt. Two weight loss steps are observed in the TGA plots. The first step occurred at a temperature of ~100 °C, which may have resulted from the sample's residual solvent or surface moisture evaporating. [24] The breakdown of the primary chain of polymers is responsible for the second stage of weight loss, which is seen in the temperature range of 380–450 °C. [25] Polymer blend electrolytes have been shown to have adequate thermal stability (~380 °C) for their possible use as an electrolyte material in lithium-ion rechargeable batteries.

The Dynamic mechanical analysis (DMA) curve of the PE20 is shown in **Figure 5(b)**. The storage modulus of the PE20 sample is ~ 750 MPa at room temperature, decreasing to ~360 MPa at 70 °C, which is near the melting point of the blend. A sharp decline in storage modulus is observed at higher temperatures, indicating substantial changes in the material's mechanical properties. In comparison, PVDF-HFP exhibits a higher storage modulus of ~900 MPa at room temperature. [26] The presence of PVP in the blend restricts polymer chain mobility, which contributes to the observed variations in the storage modulus of the blend. [27] This constraint impacts the composite's relaxing behavior. PVP specifically causes a decrease in molecular mobility, which causes the relaxation process to proceed in the composite samples at a lower temperature than in pure polymers.

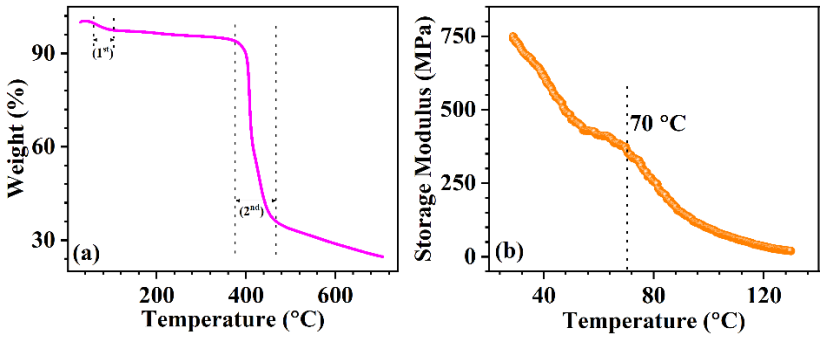

Figure 5 (a) TGA plot and (b) storage modulus vs. temperature curve of PE20 membrane.

A DC polarization study was performed using lithium as the Li^+-conducting electrode to assess the contribution of lithium-ion conductivity to the overall conduction in the PE20 sample. The Li-ion transference number was calculated using the Bruce-Vincet method mentioned in the supplementary information (equation S2). [28] The PE20 polymer electrolyte exhibited a high lithium-ion transference number of ~0.44 at room temperature (**Figure 6(a) and (b)**). This enhanced Li-ion transference number can be attributed to the "assisted Li-ion diffusion" mechanism, where lithium ions are transported between anions of the lithium salts via binding sites. [29] Furthermore, strong interactions between the lithium salt anions and the carbonyl oxygen groups/C-F in the polymer may also contribute to the increased lithium-ion transference number. [30] The electrochemical stability window of PE20 was evaluated through linear sweep voltammetry (LSV). For LSV measurement, the PE20 film was positioned between a stainless-steel spacer (serving as the working electrode) and lithium foil (acting as the reference and counter electrode) in a coin cell CR2032 configuration. The experiment was conducted at a slow scan rate of 0.1 mV S^{-1}. A significant change in current was observed at 4.53 V, and no noticeable redox currents were detected across the entire testing voltage range (**Figure 6(c)**). This indicates that the electrolyte maintains its electrochemical stability over a wide voltage window.

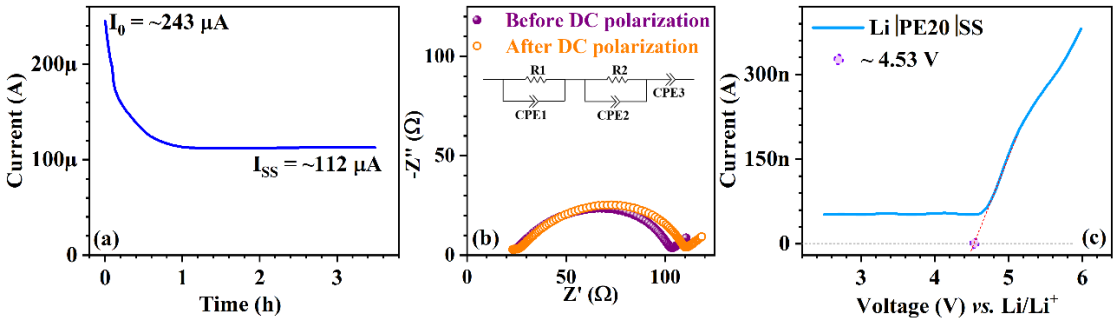

Figure 6 (a) Chronoamperometry profile of PE20 with symmetric Li||Li assembly, (b) the impedance data before and after DC polarization of Li||Li cell, and (c) LSV curve with a scan rate of 0.1 mV s^{-1}.

The stability of PE20, when paired with a lithium metal anode, is crucial for the performance of high-energy-density batteries. Interfacial stability experiments were conducted in an argon-filled glove box, where the PE20 film remained in contact with lithium metal at room temperature for 50 days without any noticeable changes (Figure S6). To assess the stability of the lithium/electrolyte interface, the lithium metal was removed by rinsing with methanol multiple times. The solid membrane was dried and analyzed using XRD and FTIR spectroscopy. The characteristic XRD and FTIR peaks of PE20 were preserved, demonstrating the film's chemical stability in contact with lithium metal (Figure S7 and S8).

The long-term electrochemical cycling stability of PE20 was further evaluated through experiments conducted on symmetrical cells. **Figure 7** illustrates the cycling performance of Li|PE20|Li symmetrical cells at a current density of 1 mA cm^{-2} at 35 °C, demonstrating excellent cycling stability for over 1500 cycles with a nearly constant polarization voltage of ~0.1 V. Additionally, long-term cycling at high current densities of 2 and 3 mA cm^{-2} was sustained for more than 200 cycles, maintaining a constant capacity of 0.25 mAh (0.125 mAh cm^{-2}) and a stable voltage response at ~22 mV and ~45 mV, respectively (Figure S9). Throughout these tests, no signs

of micro short-circuiting are noticed in the voltage profile, indicating effective suppression of dendritic lithium formation. After long-term cycling, EIS was conducted on Li||Li cells over a frequency range of 1 Hz to 1 MHz (Figure S10). The observed resistance was ~125 Ω from the Nyquist plot. Therefore, the enhanced reversibility and cycle stability of lithium plating/stripping can be ascribed to this stable interface chemistry.

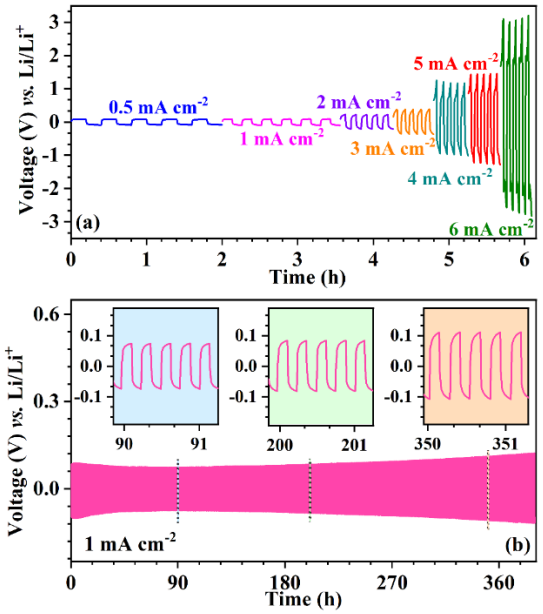

Figure 7 (a) GCD profile of a symmetric cell at different current densities and (b) long-term charge-discharge cycling of Li|PE20|Li cell at a constant areal current density of 1 mA cm^{-2}.

To further validate the electrochemical performance, Li|PE20|$LiFePO_4$ cells were assembled. The rate capability of the full-cell, along with its galvanostatic charge-discharge curves, at various C rates ranging from 0.1C to 7C, are depicted in **Figure 8(a-d)**. An increase in discharge rates leads to a reduction in discharge-specific capacity (Dis. Sp. Capacity). However, when the discharge rate decreased again, the cell reverted to its original discharge capabilities, signifying a reversible capacity loss associated with limitations in Li-ion ion diffusion rates at elevated C rates. At 0.1C (= 12.8 mA g^{-1}), the cell exhibited an initial discharge capacity of ~164 mAh g^{-1}, which dropped to ~40 mAh g^{-1} at 7C. Even at a discharge rate of 5C, the cell exhibits an impressive discharge

capacity of around 70 mAh g^{-1}. The cyclic performance of the full cell, as shown in Fig. 8(c), demonstrates stable cycling at 5C. The cell retains over ~97% of its initial specific capacity after 200 cycles, with coulombic efficiencies (C. E.) exceeding >99% throughout all cycles. Figure S11 shows the energy efficiency of the cell cycled at 5C. The energy efficiency values for the cell were 81.8% during the 1st cycle and 81.3% after the 210th cycle.

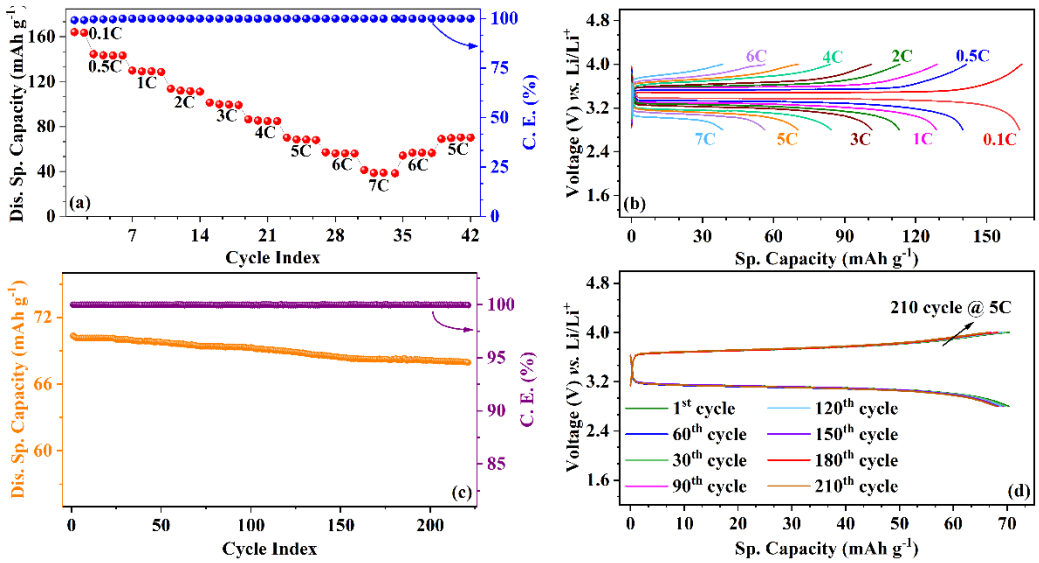

Figure 8 *GCD performance characteristics of the Li|PE20|$LiFePO_4$ cell: (a) rate performance, (b) room temperature charge-discharge curves at various C-rates, (c) cyclic stability and C. E. (%) at 5C, and (d) long-term charge-discharge cycles at room temperature at 5C.*

3. Conclusions

In conclusion, the PVDF-HFP/PVP (75:25) polymer blend electrolyte membrane was fabricated via a solution casting method. The XRD, FT-IR, and SEM analyses confirmed the complete miscibility of the salt within the polymer blend. Thermal stability of the polymer membrane was evidenced by the TGA data indicating stability up to 380 °C. The strong interaction between PVDF-HFP's large polar groups and PVP promotes the development of a high-density entangled structure, which enhances the resulting blend's mechanical characteristics and yields an excellent

tensile strength of 750 MPa at RT. EIS assessments revealed an excellent room temperature ionic conductivity of 2.84×10^{-4} S cm^{-1} and an activation energy of ~0.39 eV, indicating efficient ionic transport. The Li-ion transference number was found to be ~0.44. The electrochemical stability window of ~4.53 V further highlighted the suitability of PE20 for high-voltage applications. Furthermore, the symmetric cell tests exhibited excellent cycling stability over 1500 cycles at 1 mA cm^{-2}, confirming interfacial stability with Li metal. The full cell with LFP cathode showed a specific capacity of ~164 mAh g^{-1} at 0.1C and 70 mAh/g at 5C, maintaining charge-discharge cycle stability with minimal energy loss of about 0.5% over 200 cycles. The findings affirmed the potential of the PE20 polymer electrolyte membrane for fast-charging lithium-ion battery applications, emphasizing its mechanical, thermal, and electrochemical robustness.

4. Synthesis and Characterization

4.1. Preparation of polymer electrolyte

PVDF-HFP/PVP (75:25) blend polymers were prepared *via* the simple solution-casting method. The salt used for the polymer electrolyte solution was lithium bis(trifluoro sulfonyl)imide (LiTFSI). Lithium salt in varying proportions (PE*x*, where *x* = 0 wt%, 5 wt%, 10 wt%, 15 wt%, 20 wt%, and 25 wt% lithium salt content, denoted as PE0, PE05, PE10, PE15, PE20, and PE25, respectively) was incorporated into the polymer electrolytes. The solutions were stirred for 6 h to ensure a homogeneous blend. The solutions were then poured into Petri dishes and placed in a vacuum oven at 80 °C for 12 h to remove any residual dimethylformamide solvent. The resulting free-standing films (the thickness is 60 μm for PE0 and 120 μm for PE05 to PE25) were punched into 16 mm discs. The membranes were kept in a glove box with O_2 and H_2O levels regulated <0.1 ppm to safeguard against moisture.

4.2. Preparation of $LiFePO_4$ electrode

PVDF was dissolved in N-methyl pyrrolidinone (NMP) to formulate the binder solution. A mixture of $LiFePO_4$ (LFP), carbon black (Ketjen black), and the binder solution was combined in a 75:15:10 ratio and stirred until a uniform suspension was achieved, which was then coated onto aluminium foil using an automatic film coater. The coated electrode was dried in a vacuum oven at 120 °C for 12 h to eliminate the NMP solvent. After drying, the electrode was punched into disks with a diameter of 12 mm, yielding a mass loading of ~3.5 mg cm^{-2}.

4.3. Material characterizations

X-ray diffraction (XRD) data of the PE*x* films was collected using an Empyrean - Malvern Panalytical diffractometer, employing Cu-Kα radiation. The scanning was conducted over a 2θ range from 10 to 60° in increments of 0.02°. Fourier-transform infrared (FTIR) spectroscopy of the solid polymer membranes was conducted using PerkinElmer Spectrum IR (Spectrum Two) equipment, scanning from 4000 to 400 cm^{-1}. The morphological characteristics of the polymer samples were examined using a field emission scanning electron microscope (FE-SEM) (model: JEOL-7610+). Energy dispersive X-ray spectroscopy (EDS) was employed for elemental mapping to assess the distribution of elements in the synthesized samples.

To assess ionic conductivity, electrochemical impedance spectroscopy (EIS) was carried out using stainless steel (SS) as blocking electrodes with an LCR meter (NF Corp. ZM2376), and the impedance data were fitted using EIS analyzer software. [31] The thermal stability of the membranes was evaluated through thermogravimetric analysis with a PerkinElmer Simultaneous Thermal Analyzer (model: STA 8000), with measurements taken from 30 to 710 °C at a heating

rate of 10 °C min^{-1}. Dynamic mechanical analysis (DMA) was performed with a PerkinElmer (DMA-8000) to investigate the temperature-dependent segmental dynamics of the polymer chains.

To evaluate the electrochemical stability window of the polymer electrolyte, linear sweep voltammetry (LSV) was performed on Li|PE25|SS cell with a Keithley source meter (model 2450-EC), scanning from 2.5 to 6.0 V (vs Li^+/Li) at a rate of 0.1 mV s^{-1}. Lithium-ion transference numbers and cycling behavior were analyzed using Li|PE25|Li symmetric cells, where the transference number was determined through DC polarization and AC impedance. Symmetric and full cells (Li|PE25|LFP) were tested in CR2032 coin cells using a Neware multichannel battery testing system, and all cells were allowed to rest for 24 h before electrochemical measurements to form interphase layers between electrodes and electrolyte.

Declaration of competing interest

The authors declare that they have no known competing financial interests or personal relationships that could have appeared to influence the work reported in this paper.

Acknowledgments

SK thanks the Science and Engineering Research Board (SERB) for the Core Research Grant (Grant no. CRG/2021/005548). The Ministry of Education is also gratefully acknowledged for funding (Grant no. MoE-STARS/STARS-2/2023-0365).

References

[1] a)Y. Ding, Z. P. Cano, A. Yu, J. Lu, Z. Chen, *EER* **2019**, *2*, 1-28; b)Y. Tian, G. Zeng, A. Rutt, T. Shi, H. Kim, J. Wang, J. Koettgen, Y. Sun, B. Ouyang, T. Chen, Z. Lun, Z. Rong, K. Persson, G. Ceder, *Chem. Rev.* **2021**, *121*, 1623-1669.

[2] S. Wang, G. P. Demopoulos, *Energy Storage Mater.* **2024**, *71*, 103604.

[3] a)M. Li, M. Feng, D. Luo, Z. Chen, *CRPS* **2020**, *1*; b)J. Duan, X. Tang, H. Dai, Y. Yang, W. Wu, X. Wei, Y. Huang, *EER* **2020**, *3*, 1-42; c)T. R. Tanim, E. J. Dufek, M. Evans, C.

Dickerson, A. N. Jansen, B. J. Polzin, A. R. Dunlop, S. E. Trask, R. Jackman, I. Bloom, Z. Yang, E. Lee, *J. Electrochem. Soc.* **2019**, *166*, A1926.

[4] a)C.-Y. Wang, T. Liu, X.-G. Yang, S. Ge, N. V. Stanley, E. S. Rountree, Y. Leng, B. D. McCarthy, *Nature* **2022**, *611*, 485-490; b)M. Xia, M. Lin, G. Liu, Y. Cheng, T. Jiao, A. Fu, Y. Yang, M. Wang, J. Zheng, *Chem. Eng. J.* **2022**, *442*, 136351.

[5] a)P. Albertus, S. Babinec, S. Litzelman, A. Newman, *Nat. Energy* **2018**, *3*, 16-21; b)D. Lu, Y. Shao, T. Lozano, W. D. Bennett, G. L. Graff, B. Polzin, J. Zhang, M. H. Engelhard, N. T. Saenz, W. A. Henderson, P. Bhattacharya, J. Liu, J. Xiao, *Adv. Energy Mater.* **2015**, *5*, 1400993.

[6] a)J. M. Tarascon, M. Armand, *Nature* **2001**, *414*, 359-367; b)R. Chen, Q. Li, X. Yu, L. Chen, H. Li, *Chem. Rev.* **2020**, *120*, 6820-6877; c)R. S. Longchamps, X.-G. Yang, C.-Y. Wang, *ACS Energy Lett.* **2022**, *7*, 1103-1111.

[7] a)P. Gami, M. Badole, H. N. Vasavan, A. K. Das, S. Saxena, N. Dagar, V. Srihari, S. Kumar, *J. Power Sources* **2024**, *618*, 235214; b)A. K. Das, M. Badole, H. N. Vasavan, S. Saxena, P. Gami, N. Dagar, S. Kumar, *J. Energy Storage* **2024**, *94*, 112452; c)P. Gami, A. K. Das, M. Badole, H. N. Vasavan, S. Saxena, N. Dagar, S. Deswal, P. Kumar, A. Dwivedi, H. K. Poswal, S. Kumar, *Ceram. Int.* **2024**.

[8] a)D. Zhou, D. Shanmukaraj, A. Tkacheva, M. Armand, G. Wang, *Chem* **2019**, *5*, 2326-2352; b)L. Long, S. Wang, M. Xiao, Y. Meng, *J. Mater. Chem. A* **2016**, *4*, 10038-10069; c)Z. Song, F. Chen, M. Martinez-Ibañez, W. Feng, M. Forsyth, Z. Zhou, M. Armand, H. Zhang, *Nat. Commun.* **2023**, *14*, 4884; d)J. C. Barbosa, R. Gonçalves, C. M. Costa, S. Lanceros-Méndez, *ACS Omega* **2022**, *7*, 14457-14464; e)J. Li, Y. Cai, H. Wu, Z. Yu, X. Yan, Q. Zhang, T. Z. Gao, K. Liu, X. Jia, Z. Bao, *Adv. Energy Mater.* **2021**, *11*, 2003239; f)X. Zhang, S. Liu, Y. Zheng, X. Koh, Q. F. Lim, M. Sharma, D. W. H. Fam, *Mater. Lett.* **2021**, *294*, 129789.

[9] a)J. Lopez, D. G. Mackanic, Y. Cui, Z. Bao, *Nat. Rev. Mater.* **2019**, *4*, 312-330; b)N. Yazie, D. Worku, N. Gabbiye, A. Alemayehu, Z. Getahun, M. Dagnew, *Mater. Renew. Sustain. Energy.* **2023**, *12*, 73-94; c)B. Liang, Q. Jiang, S. Tang, S. Li, X. Chen, *J. Power Sources* **2016**, *307*, 320-328.

[10] a)H. Zhang, F. Chen, J. Carrasco, *Energy Storage Mater.* **2021**, *36*, 77-90; b)A. K. Das, M. Badole, H. N. Vasavan, S. Saxena, P. Gami, N. Dagar, S. Kumar, *Energy Fuels* **2024**, *38*, 11253-11261; c)J. Atik, D. Diddens, J. H. Thienenkamp, G. Brunklaus, M. Winter, E. Paillard, *Angew. Chem., Int. Ed.* **2021**, *60*, 11919-11927.

[11] H. Huo, B. Wu, T. Zhang, X. Zheng, L. Ge, T. Xu, X. Guo, X. Sun, *Energy Storage Mater.* **2019**, *18*, 59-67.

[12] a)H. M. Zidan, E. M. Abdelrazek, A. M. Abdelghany, A. E. Tarabiah, *J. Mater. Res. Technol.* **2019**, *8*, 904-913; b)U. Gradišar Centa, M. Mihelčič, V. Bobnar, M. Remškar, L. Slemenik Perše, *Coatings* **2022**, *12*.

[13] a)M. Teodorescu, M. Bercea, *POLYM-PLAST TECHNOL* **2015**, *54*, 923–943; b)L. K. Mireles, M. R. Wu, N. Saadeh, L. Yahia, E. Sacher, *ACS Omega* **2020**, *5*, 30461-30467.

[14] a)A. K. Das, M. Badole, H. N. Vasavan, S. Saxena, P. Gami, S. Deswal, P. Kumar, S. Kumar, *Mater. Today Sustain.* **2024**, *26*, 100758; b)A. K. Das, M. Badole, H. N. Vasavan, S. Saxena, P. Gami, S. Kumar, *Ceram. Int.* **2023**, *49*, 29719-29728; c)P. Gami, M. Badole, H. N. Vasavan, A. K. Das, S. Saxena, S. Kumar, *ACS Appl. Energy Mater.* **2024**, *2*, 1278-1287.

[15] A. Y. Yassin, *JMR&T* **2021**, *15*, 754-767.

[16] a)V. M. Mohan, V. Raja, P. B. Bhargav, A. K. Sharma, V. V. R. N. Rao, *J. Polym. Res.* **2007**, *14*, 283-290; b)K. Deshmukh, M. B. Ahamed, A. R. Polu, K. K. Sadasivuni, S. K. K. Pasha, D. Ponnamma, M. A.-A. AlMaadeed, R. R. Deshmukh, K. Chidambaram, *J. Mater. Sci.: Mater. Electron.* **2016**, *27*, 11410-11424.
[17] A. Yassin, *BJAST* **2014**, *4*, 4263-4279.
[18] D. R. Baganizi, E. Nyairo, S. A. Duncan, S. R. Singh, V. A. Dennis, *Nanomaterials (Basel)* **2017**, *7*.
[19] Shalu, S. K. Chaurasia, R. K. Singh, S. Chandra, *J. Phys. Chem. B.* **2013**, *117*, 897-906.
[20] M. Sangeetha, A. Mallikarjun, M. Jaipal Reddy, J. Siva Kumar, *IOP Conf. Ser. Mater. Sci. Eng.* **2017**, *225*, 012049.
[21] A. Narita, W. Shibayama, H. Ohno, *J. Mater. Chem.* **2006**, *16*, 1475-1482.
[22] Q. Zhou, J. Ma, S. Dong, X. Li, G. Cui, *Adv. Mater.* **2019**, *31*, 1902029.
[23] M. Singh, V. K. Singh, K. Surana, B. Bhattacharya, P. K. Singh, H.-W. Rhee, *Journal of Industrial and Engineering Chemistry* **2013**, *19*, 819-822.
[24] A. R. Polu, D. K. Kim, H.-W. Rhee, *Ion.* **2015**, *21*, 2771-2780.
[25] K. Deshmukh, M. Basheer Ahamed, S. Sankaran, S. K. Khadheer Pasha, K. Kumar Sadasivuni, D. Ponnamma, M. Al-Ali AlMaadeed, *Mater. Today Proc.* **2018**, *5*, 8744-8752.
[26] A. Dargahi, R. Schultz, J. Runka, H. Ashrafizadeh, B. Xu, H. E. Naguib, *Mater. Des.* **2023**, *232*, 112124.
[27] M. Hara, J. A. Sauer, *J. Polym. Sci., Part C* **1998**, *38*, 327-362.
[28] J. Evans, C. A. Vincent, P. G. Bruce, *Polymer* **1987**, *28*, 2324-2328.
[29] a)Z.-K. Tang, J. S. Tse, L.-M. Liu, *J. Phys. Chem. Lett.* **2016**, *7*, 4795-4801; b)Z. Li, R. Yu, S. Weng, Q. Zhang, X. Wang, X. Guo, *Nat. Commun.* **2023**, *14*, 482.
[30] a)Y. Cui, X. Liang, J. Chai, Z. Cui, Q. Wang, W. He, X. Liu, Z. Liu, G. Cui, J. Feng, *Adv. Sci.* **2017**, *4*, 1700174; b)J. Fu, X. Ji, J. Chen, L. Chen, X. Fan, D. Mu, C. Wang, *Angew. Chem., Int. Ed.* **2020**, *59*, 22194-22201.
[31] A. S. B. a. G. A. Ragoisha, in *Progress in Chemometrics Research*, Nova Science Publishers, New York, 2008.

[Supplementary Material]

PVDF-HFP/PVP-based Miscible Blend Electrolyte for Fast-Charging Lithium Metal Batteries

*Pratiksha Gami, Asish Kumar Das, Hari Narayanan Vasavan, Samriddhi Saxena, Neha Dagar, and Sunil Kumar**

Department of Metallurgical Engineering and Materials Science, Indian Institute of Technology Indore, Simrol, 453552, India.

*Corresponding author, E-mail: sunil@iiti.ac.in

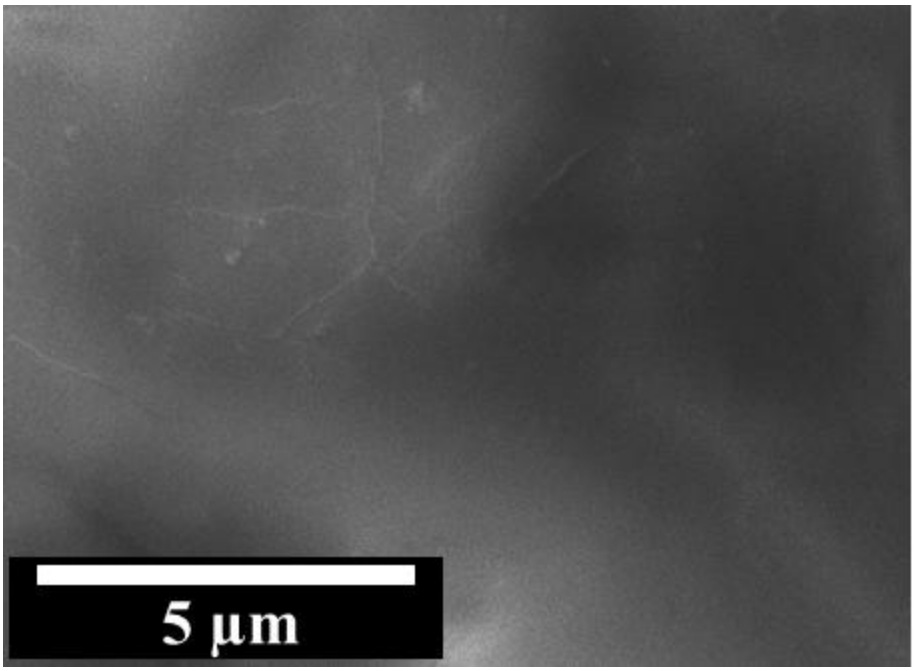

Figure S1 SEM micrograph of PE05.

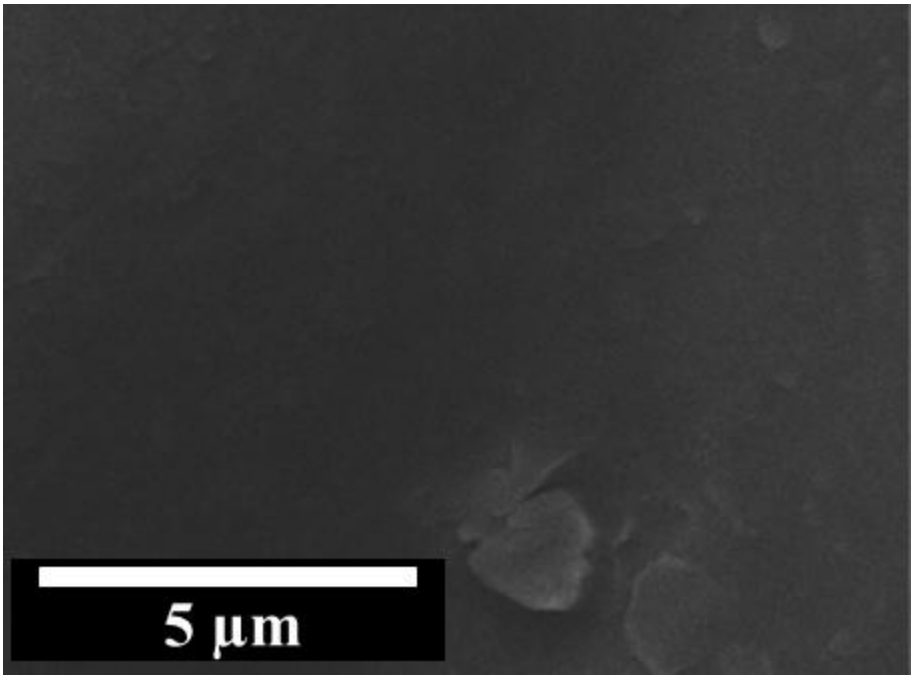

Figure S2 SEM micrograph of PE10.

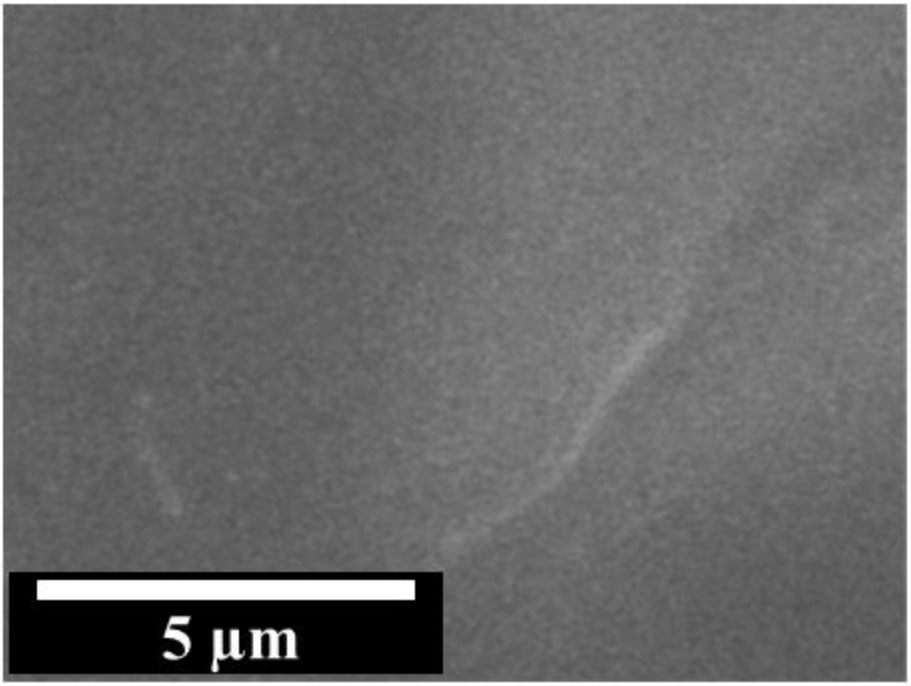

Figure S3 SEM micrograph of PE15.

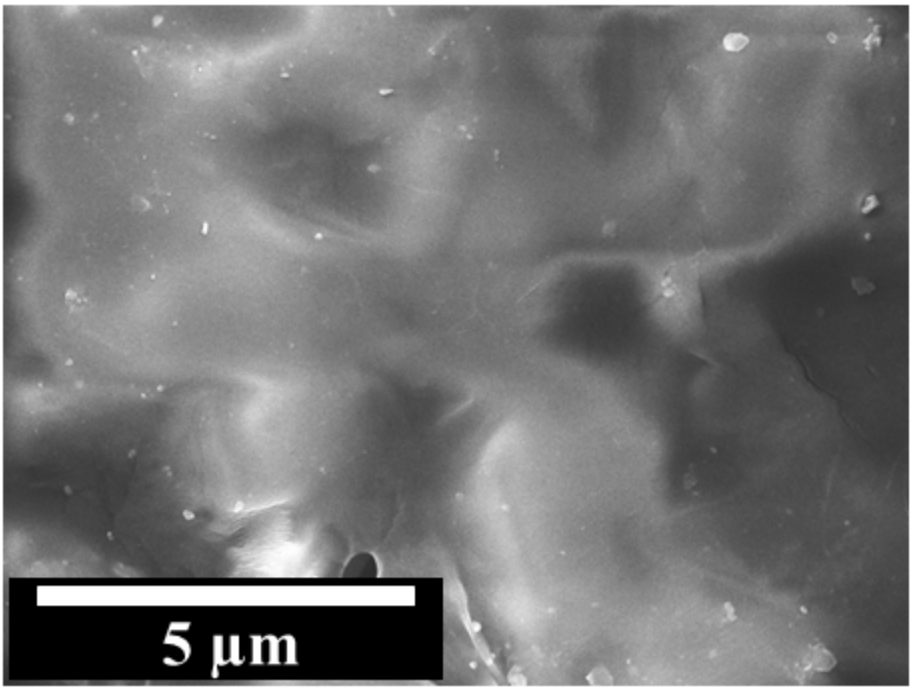

Figure S4 SEM micrograph of PE25.

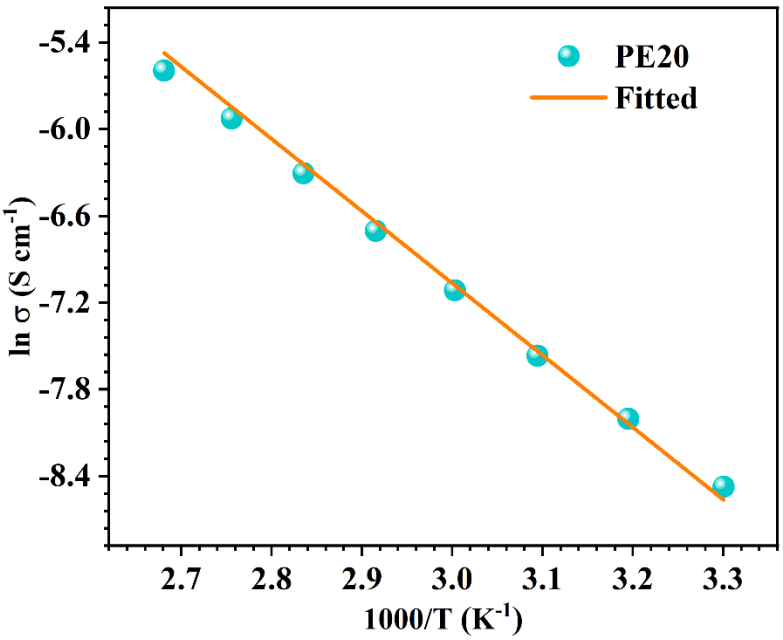

Figure S5 Arrhenius fitting of the temperature-dependent conductivity of PE20.

Figure S6 Images of Li metal before (right) and after (left) contact with PE20.

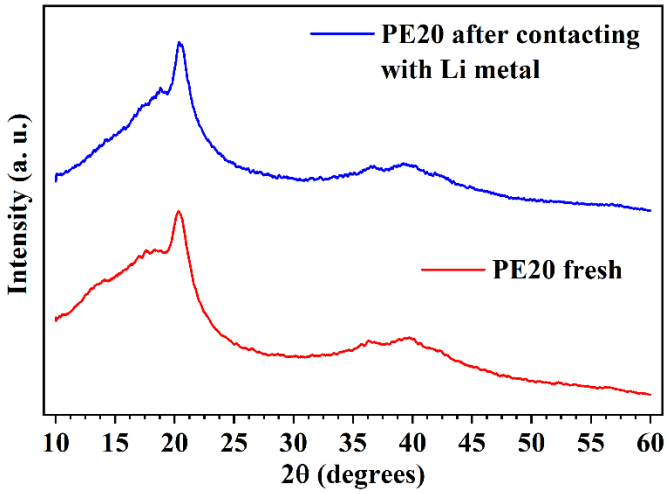

Figure S7 XRD patterns of PE20 before (fresh) and after contact with Li metal.

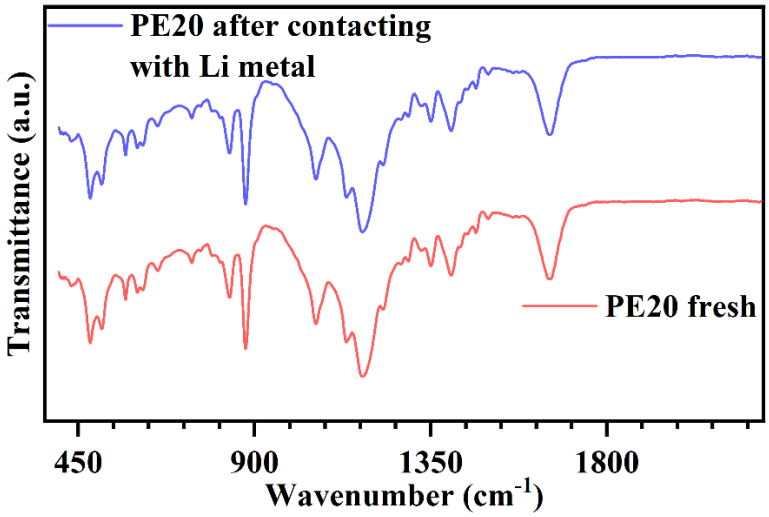

Figure S8 FTIR spectra of PE20 before (fresh) and after contact with Li metal.

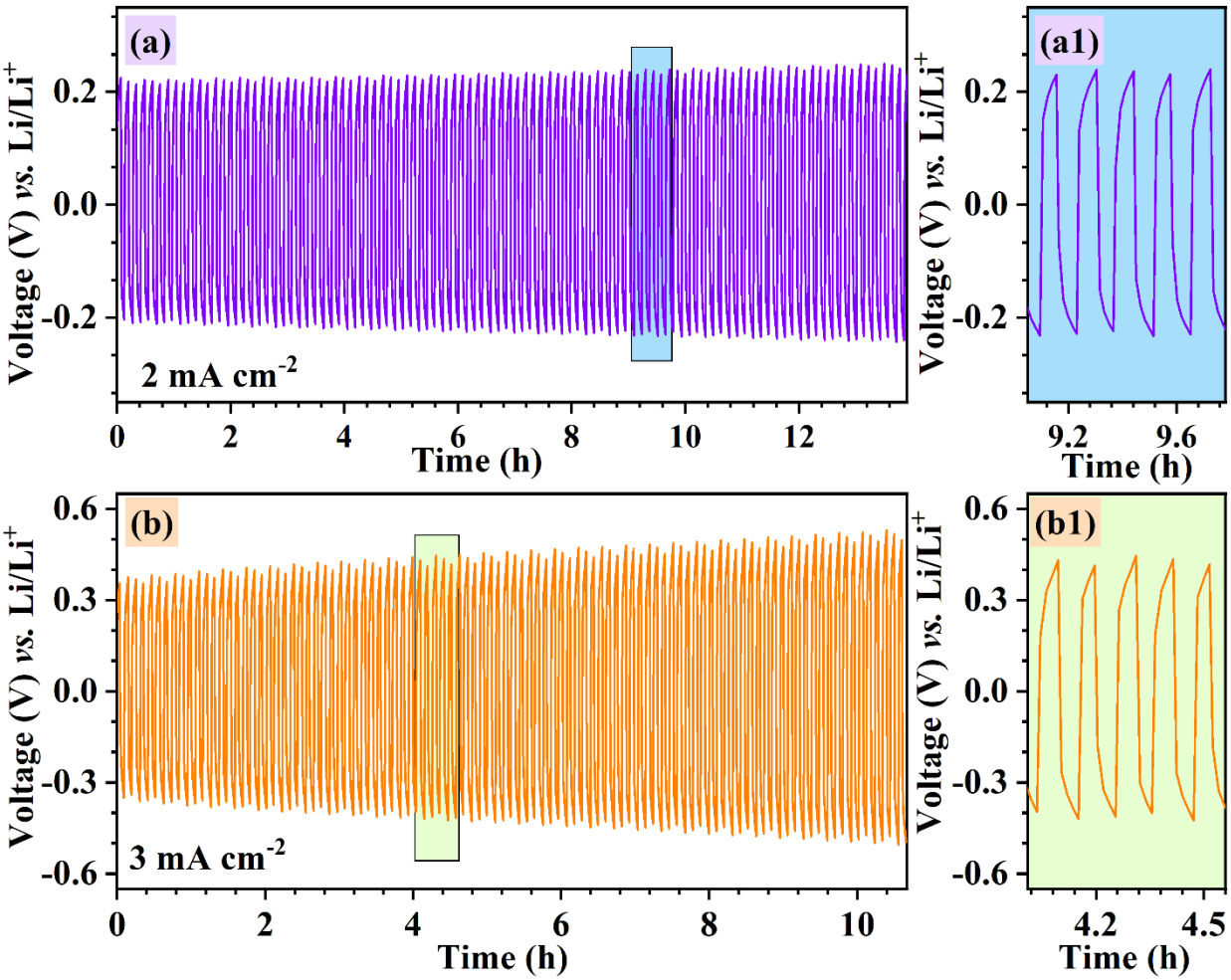

Figure S9 GCD data of symmetric cells are shown at different current densities: (a) 2 mA cm^{-2}, (a1) an enlarged view from 9.05 to 9.78 h of (a), (b) 3 mA cm^{-2} and (b1) zoomed-in view from 4.01 to 4.56 of (b).

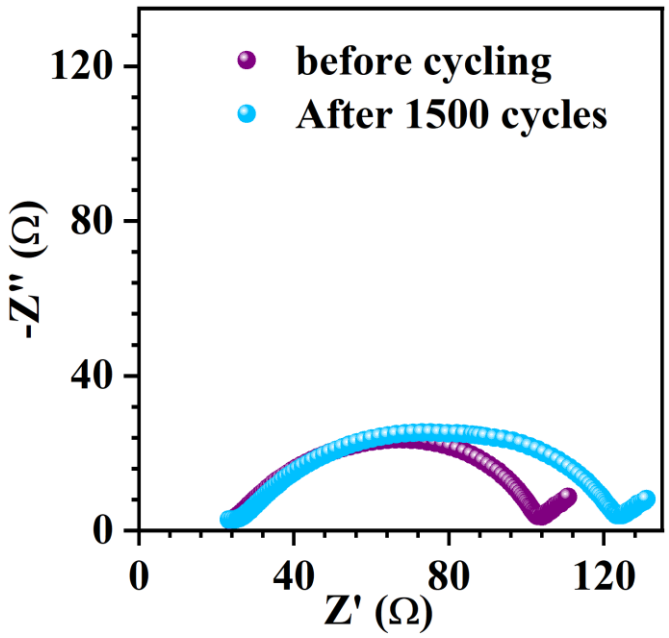

Figure S10 Nyquist plots of the symmetric cell before and after cycling.

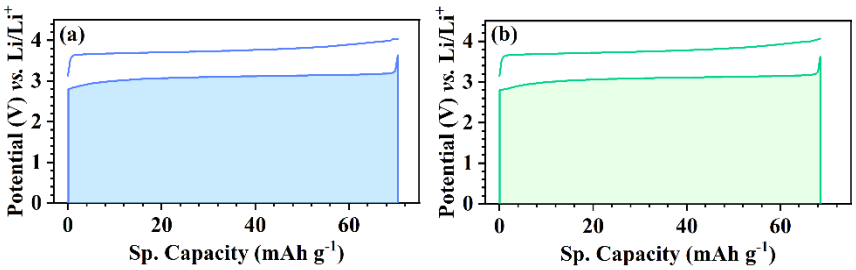

Figure S11 The energy efficiency curves of Li||LFP: (a) 1st cycle and (b) 210th cycle at 5C rate. The shaded area under the discharge curve represents the energy extracted during discharge, compared to the total energy supplied during charging (indicated by the area under the charging curve).

equation S1 *Arrhenius equation*

$$\sigma(T) = \sigma_0 e^{\left(\frac{-E_A}{k_B T}\right)}$$

Where σ_0 is a pre-exponential factor,

E_A = activation energy,

k_B = Boltzmann constant,

T = absolute temperature.

equation S2 *Li-ion transference number*

$$t_{Li^+} = \frac{I_{ss}(\Delta V - I_o R_o)}{I_o(\Delta V - I_{ss} R_{ss})}$$

Where I_{ss} (steady-state current) = 0.112 mA,

I_o (initial current) = 0.245 mA,

R_{ss} (steady-state resistance) = 109 Ω*,*

R_o (initial resistance) = 102 Ω*,*

ΔV (perturbation voltage) = 500 mV.